Synthesis of glassy Fe-Co-Nd-Zr-B alloys and their crystallization-induced magnetic properties

Materials Transactions, JIM, Vol. 39, No. 3 (1998), pp. 327 to 333

Synthesis of Glassy Fe-Co-Nd-Zr-B Alloys and Their Crystallization-Induced Magnetic Properties

A. Inoue*, K. Fujita*†, T. Zhang*
and A. Makino**

*Institute for Materials Research, Tohoku University, Sendai 980-8577, Japan
**Alps Electric Co. Ltd., Nagaoka 940-0006, Japan

A new Fe-based amorphous alloy exhibiting the glass transition and supercooled liquid region before crystallization was searched in the composition range of $Fe_{63}Co_7Nd_{10-x}Zr_xB_{20}$ (x=0 to 6 at%). The amorphous alloys containing 4 to 6 at%Zr were found to exhibit the glass transition, followed by a supercooled liquid region. The crystallization from the supercooled liquid of the 4%Zr alloy occurred through three stages of Am→Am′+Fe_3B→Am″+Fe_3B+γ-Fe+$Nd_2Fe_{23}B_3$+Fe_2Zr+Fe_3Zr→α-Fe+Fe_2Zr+Fe_3Zr+$Nd_2Fe_{14}B$+Fe_2B+ZrB_2. In the crystallized state, the 4% and 6%Zr alloys exhibited hard magnetic properties, *i.e.*, saturation magnetization of 1.15 to 1.18 T, remanence of 0.75 to 0.76 T, coercive force of 30 to 58 kA/m and maximum energy product of 7.8 to 13 kJ/m^3. The grain sizes of the α-Fe and $Nd_2Fe_{14}B$ phases for the 4%Zr alloy subjected to optimum annealing were about 45 and 25 nm, respectively. The fine mixed structure was thought to reveal the hard magnetic properties by the exchange magnetic coupling mechanism even in the coexistent state with Fe_2Zr, Fe_3Zr, Fe_2B and ZrB_2. The appearance of the glass transition also implies that the 4%Zr and 6%Zr alloys have a high glass-forming ability leading to the formation of a bulk amorphous alloy. The finding that the amorphous alloys exhibited the glass transition in the as-quenched state and the hard magnetic properties in the crystallized state is important, because the direct production of a bulk hard magnetic alloy by a simple process is expected, such as the crystallization of the cast bulk amorphous alloy.

(Received June 4, 1997; In Final Form November 5, 1997)

Keywords: *iron-based amorphous alloy, glass transition, supercooled liquid region, high glass-forming ability, multicomponent system, hard magnetic property, multistage crystallization, bulk hard magnetic alloy*

I. Introduction

It has been reported that the Pt-Ni-P[1] and Pd-Ni-P[2] amorphous alloys found in the latter 1960 s exhibit a supercooled liquid region before crystallization and are formed in the diameter range below several millimeters in the case of non-fluxed liquid[3]. However, no significant attention has been paid to these amorphous alloys because of the limitation of the noble metals. Since the recent findings of new multicomponent amorphous alloys with a wide supercooled liquid region before crystallization and a high glass-forming ability in Ln-Al-TM[4][5], Mg-Ln-TM[6][7], Zr-Al-TM[8][9], Zr-Ti(Nb or Pd)-Al-TM[10], Zr-Ti-TM-Be[11] and Pd-Cu-Ni-P[12] (Ln=lanthanide metal, TM=transition metal) systems, attention to bulk amorphous alloys has increased significantly. The supercooled liquid region defined by the difference between the glass transition temperature (T_g) and crystallization temperature (T_x), ΔT_x($=T_x-T_g$) is about 70 K for the Ln-[13] and Mg-[14] based alloys, 80 to 127 K[9] for the Zr-based alloys and about 100 K[12] for the Pd-based alloys. The high thermal stability of the supercooled liquid against crystallization produced the bulk amorphous alloys with maximum diameters of about 10 mm for the Ln-[13] and Mg-[15]based alloys, about 30 mm[16] for the Zr-based alloys and 72 mm[17] for the Pd-based alloys. It is clear that the glass-forming ability increases with increasing ΔT_x[18]-[20]. It is therefore important to search for a new amorphous alloy with a wide supercooled liquid region before crystallization in the development of bulk amorphous alloys. Based on the above-described alloy compositions with high glass-forming ability, we have proposed[18]-[23] the three empirical rules for the achievement of high glass-forming ability, *i.e.*, (1) multicomponent system consisting of more than three elements, (2) significant difference of the atomic size ratios above about 12%, and (3) negative heats of mixing. In the framework of the three empirical rules, we have searched for ferromagnetic amorphous alloys with a wide supercooled liquid region and a high glass-forming ability in Fe- and Co-based systems. As a result, two kinds of Fe-based amorphous alloys as Fe-(Al, Ga)-(P, C, B, Si)[24][25] and Fe-(Co, Ni)-(Zr, Hf, Nb)-B[26]-[28] systems were found to exhibit a wide supercooled liquid region of 50 to 90 K and a high glass-forming ability with maximum diameters up to 6 mm. These bulk amorphous alloys exhibit good soft magnetic properties of 0.9 to 1.2 T for saturation magnetization, 1 to 7 A/m for coercive force and 7000 to 25000 for permeability at 1 kHz at room temperature. However, there has been no datum on a bulk amorphous alloy in Fe-based systems containing Ln elements[29]. Recently, good hard magnetic properties have been obtained for crystalline Fe-Nd-B alloys containing a large amount of B (18 to 20 at%)[30][31]. If Fe-Ln base

† Permanent address: Alps Electric Co. Ltd., Nagaoka 940-0006, Japan.

bulk amorphous alloys can be synthesized by a casting process, the subsequent crystallization of the bulk amorphous alloys is expected to enable the preparation of a bulk hard magnetic material. This paper is intended to examine the possibility of forming an amorphous alloy with glass transition in $Fe_{63}Co_7Nd_{10-x}Zr_xB_{20}$ system and to present the relation between the crystallized structure and magnetic properties of the amorphous alloys.

II. Experimental Procedure

Multicomponent alloys with composition $Fe_{80-x}Nd_xB_{20}$ (x=0 to 10 at%), $Fe_{70-x}Co_xNd_{10}B_{20}$ (x=0 to 20 at%) and $Fe_{63}Co_7Nd_{10-x}Zr_xB_{20}$ (x=0 to 6 at%) were examined in the present study. The alloy ingots were prepared by arc melting the mixtures of pure Fe, Co, Nd and Zr metals and pure B crystal in an argon atmosphere. The alloy compositions represent the nominal atomic percentages of the mixtures. Rapidly solidified ribbons of 0.02 mm in thickness and 1.0 mm in width were prepared by a single-roller melt spinning equipment in an argon atmosphere. The amorphous nature and crystallized structure were examined by X-ray diffractometry and transmission electron microscopy (TEM). Thermal stability associated with glass transition, supercooled liquid and crystallization was examined at a heating rate of 0.67 K/s by differential scanning calorimetry (DSC). Magnetic properties of saturation magnetization and coercive force were examined with a vibrating sample magnetometer (VSM) under a maximum applied magnetic field of 1256 kA/m at room temperature.

III. Results

An amorphous single phase is formed in $Fe_{75}Nd_5B_{20}$, $Fe_{75-x}Co_xNd_5B_{20}$ (x=0 to 20 at%), $Fe_{70}Nd_{10}B_{20}$ and $Fe_{70-x}Co_xNd_{10}B_{20}$ (x=0 to 20 at%) by melt spinning. Figure 1 shows DSC curves of the melt-spun $Fe_{70-x}Co_xNd_{10}B_{20}$ (x=0, 7 and 15 at%) and $Fe_{60}Co_{15}Nd_5B_{20}$ amorphous alloys. Distinct exothermic peaks due to crystallization are observed in the temperature range of 820 to 1100 K for all the alloys. However, no appreciable glass transition is observed in the temperature range below T_x.

Since the glass transition and supercooled liquid region in the temperature range below T_x have been reported for $Fe_{63}Co_7Zr_{10}B_{20}$[26] and $Fe_{63}Co_7Nb_{10}B_{20}$[27] amorphous alloys, the effect of Nd and Zr or Nb on the thermal stability was examined. Figure 2 shows X-ray diffraction patterns of the melt-spun $Fe_{63}Co_7Nd_{10-x}Zr_xB_{20}$ (x=0, 2, 4 and 6 at%) alloys. The X-ray diffraction patterns consist only of a broad peak and the wave vector ($K_p=4\pi \sin\theta/\lambda$) of the broad peak increases gradually from 28.6 nm^{-1} to 30.2 nm^{-1} with increasing Zr content, indicating that the interatomic spacing between Fe atoms decreases by the dissolution of Zr. Figure 3 shows DSC curves of the amorphous $Fe_{63}Co_7Nd_{10-x}Zr_xB_{20}$ (x=0 to 6 at%) alloys. Although no glass transition is observed for the 0%Zr and 2%Zr alloys, the 4 at%Zr alloy shows a slight endothermic reaction at the temperature just below T_x and

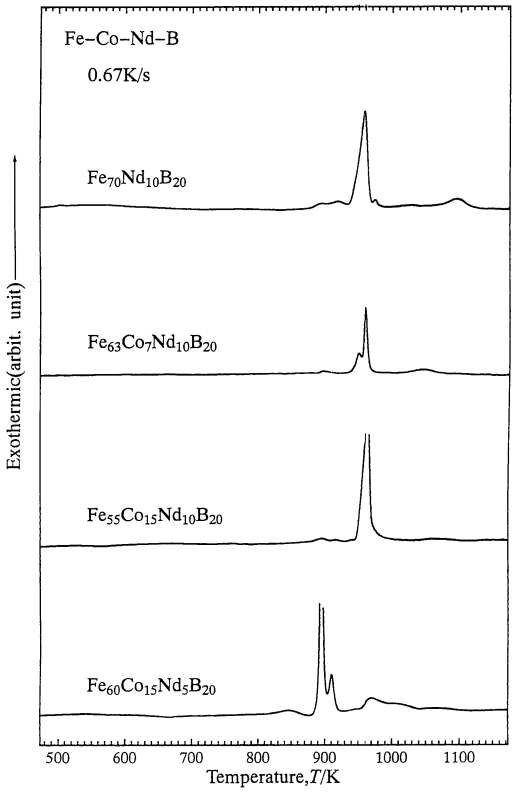

Fig. 1 DSC curves of the melt-spun $Fe_{70-x}Co_xNd_{10}B_{20}$ (x=0, 7 and 15) and $Fe_{60}Co_{15}Nd_5B_{20}$ alloys.

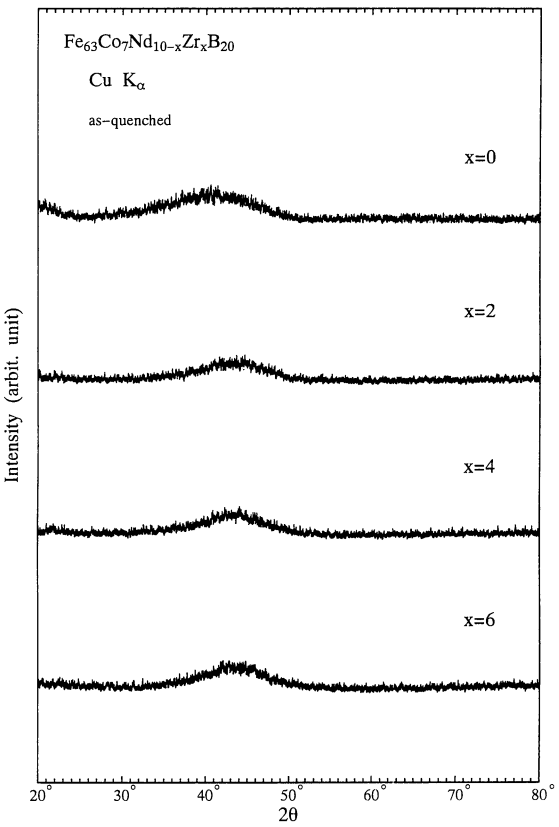

Fig. 2 X-ray diffraction patterns of the melt-spun $Fe_{63}Co_7Nd_{10-x}Zr_xB_{20}$ (x=0, 2, 4 and 6) alloys.

the endothermic reaction becomes significant for the 6 at%Zr alloy. As shown in Fig. 3, the T_g and T_x are, respectively, 844 and 877 K for the 4 at% Zr alloy and 839 and 880 K for the 6 at%Zr alloy and the resulting ΔT_x value is evaluated to be 33 and 41 K, respectively. The replacement of Nd by Nb also causes the formation of an amorphous single phase for the alloy series of $Fe_{63}Co_7Nd_{10-x}Nb_xB_{20}$, but no appreciable glass transition is observed.

Among the three kinds of alloy series $Fe_{80-x-y}Co_xNd_yB_{20}$, $Fe_{63}Co_7Nd_{10-x}Zr_xB_{20}$ (x=0 to 6 at%) and $Fe_{63}Co_7Nd_{10-x}Nb_xB_{20}$ (x=0 to 6 at%), it should be noticed that only the amorphous alloys containing 4 to 6 at%Zr exhibit the glass transition, followed by a supercooled liquid region and then four exothermic peaks (Fig. 3). Considering that the precipitations of α-Fe and $Nd_2Fe_{14}B$ phases are expected to result in the hard magnetic properties it is important to examine the crystallized structures corresponding to each exothermic peak for the Zr-containing amorphous alloys with glass transition. Figures 4 and 5 show X-ray diffraction patterns of the $Fe_{63}Co_7Nd_6Zr_4B_{20}$ and $Fe_{63}Co_7Nd_4Zr_6B_{20}$ alloys annealed for 300 s in the supercooled liquid region and at the temperatures just above the first, second and fourth peaks. The X-ray diffraction peaks of the 4%Zr alloy were identified to consist of Fe_3B for the first exothermic peak, $Fe_3B+\gamma$-Fe+$Nd_2Fe_{23}B_3+Fe_2Zr+Fe_3Zr$ for the second peak and α-Fe+$Fe_2Zr+Fe_3Zr+Nd_2Fe_{14}B+Fe_2B+ZrB_2$ for the third peak. Similarly, the crystallized structure of the 6%Zr alloy is composed of Fe_3B for the first exothermic peak, $Fe_3B+\gamma$-Fe+α-Fe+$Nd_2Fe_{23}B_3+Fe_2Zr$ for the second peak and α-Fe+$Nd_2Fe_{14}B+NdFe_4B_4+Fe_2Zr+Fe_2B+ZrB_2$ for the third peak. It is therefore summarized that the crystallization reaction occurs mainly through the following three stages of Am→Am′+Fe_3B→Am″+$Fe_3B+\gamma$-Fe+$Nd_2Fe_{23}B_3+Fe_2Zr+Fe_3Zr$ → α-Fe+$Fe_2Zr+Fe_3Zr+Nd_2Fe_{14}B+Fe_2B+ZrB_2$ for the 4%Zr alloy and Am→Am′+Fe_3B→Am″+$Fe_3B+\gamma$-Fe+α-Fe+$Nd_2Fe_{23}B_3+Fe_2Zr$→α-Fe+$Nd_2Fe_{14}B+NdFe_4B_4+Fe_2Zr+Fe_2B+ZrB_2$ for the 6%Zr alloy. The Fe_3B, γ-Fe and $Nd_2Fe_{23}B_3$ phases precipitate as intermediate metastable phases and the main crystalline phases consist of α-Fe, Fe_2Zr, ZrB_2 and $Nd_2Fe_{14}B$, which are significantly different from those ($Fe_3B+Nd_2Fe_{14}B+\alpha$-Fe) for $Fe_{75}Nd_5B_{20}$ alloy. Thus, the addition of 4 to 6 at%Zr induces the precipitation of Fe_2Zr and ZrB_2 phases and the disappearance of Fe_3B.

Figure 6 shows the saturation magnetization (I_s), remanence (I_r), intrinsic coercive force ($_iH_c$) and maximum energy product $(BH)_{max}$ as a function of annealing temperature (T_a) for the amorphous $Fe_{63}Co_7Nd_6Zr_4B_{20}$ and $Fe_{63}Co_7Nd_4Zr_6B_{20}$ alloys. These alloys exhibit the hard magnetic characteristics in the fully crystallized state,

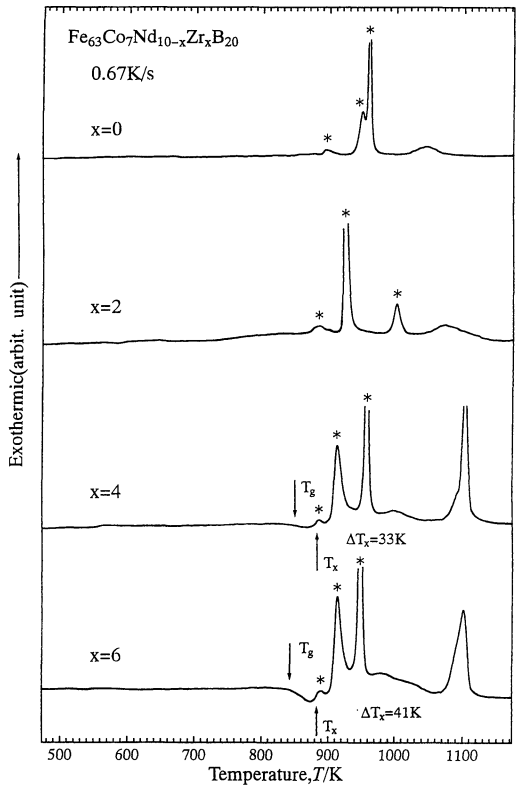

Fig. 3 DSC curves of amorphous $Fe_{63}Co_7Nd_{10-x}Zr_xB_{20}$ (x=0, 2, 4 and 6) alloys. The asterisks denote the peaks due to the precipitation of crystalline phases from the amorphous phase.

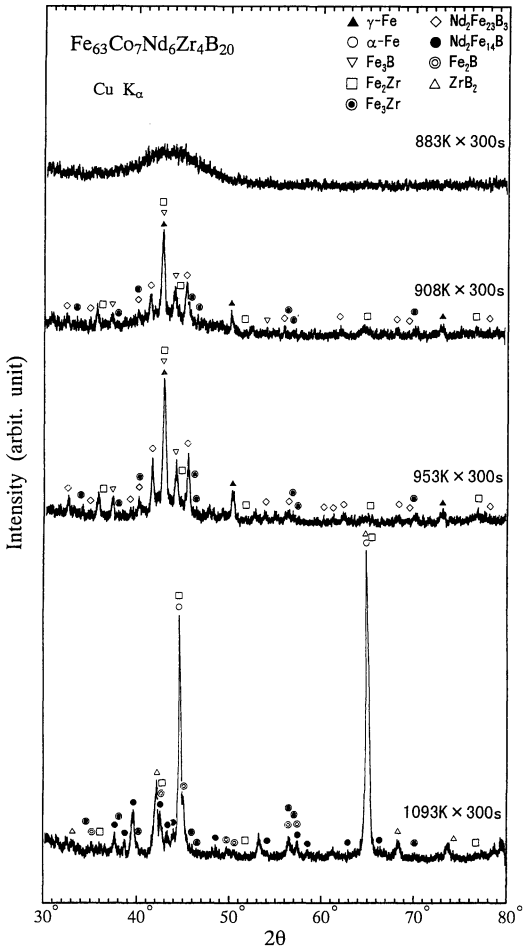

Fig. 4 X-ray diffraction patterns of the amorphous $Fe_{63}Co_7Nd_6Zr_4B_{20}$ alloy annealed for 300 s at 883 K, 908 K, 953 K and 1093 K.

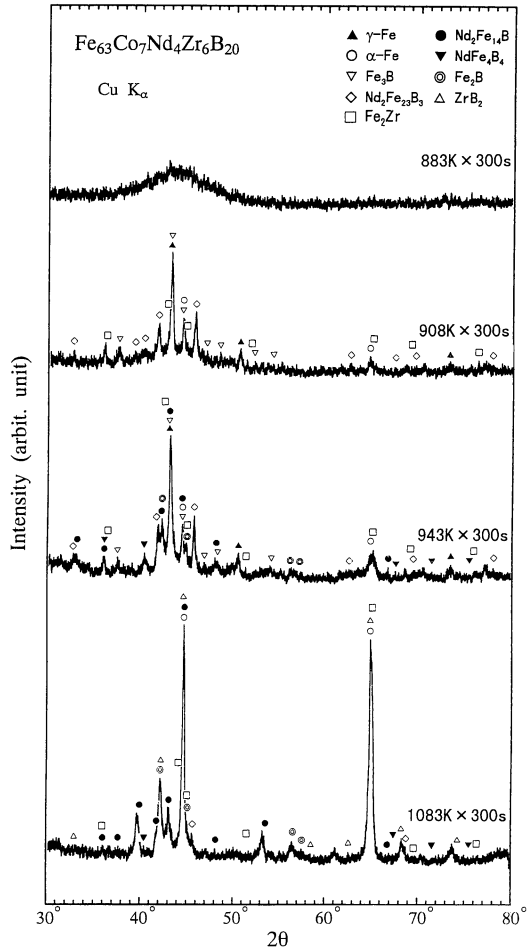

Fig. 5 X-ray diffraction patterns of the amorphous $Fe_{63}Co_7Nd_4Zr_6B_{20}$ alloy annealed for 300 s at 883 K, 908 K, 943 K and 1083 K.

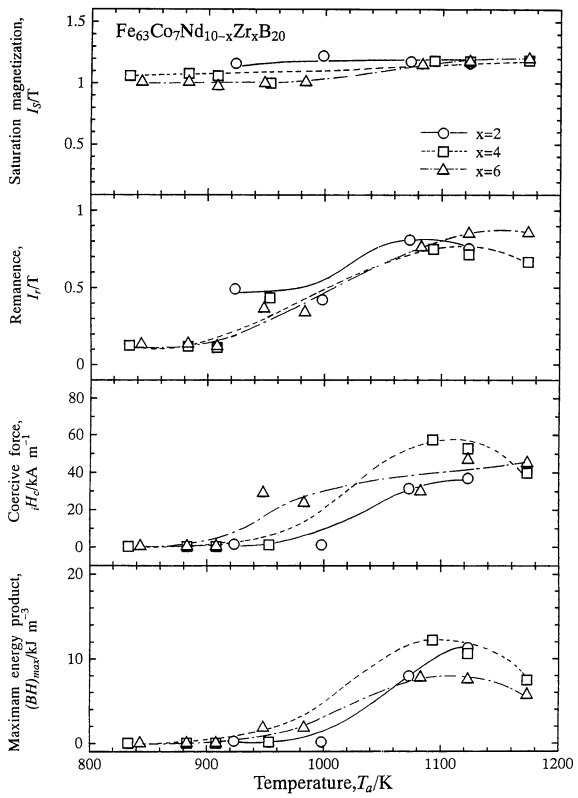

Fig. 6 Changes in maximum magnetic flux density (I_s), remanence (I_r), intrinsic coercive force ($_iH_c$) and maximum energy product $(BH)_{max}$ as a function of annealing temperature for amorphous $Fe_{63}Co_7Nd_{10-x}Zr_xB_{20}$ (x=2, 4 and 6) alloys.

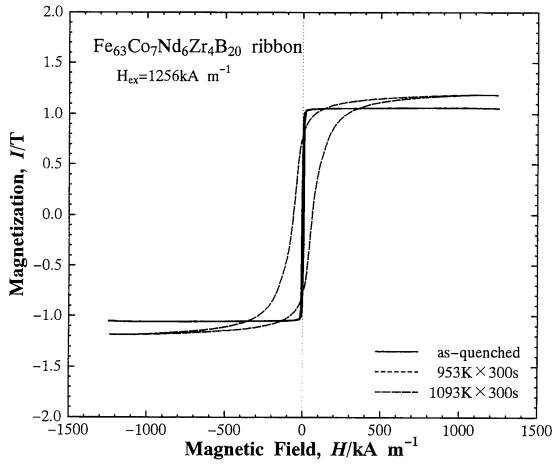

Fig. 7 Hysteresis I-H curves of an amorphous $Fe_{63}Co_7Nd_6Zr_4B_{20}$ alloy at as-quenched and annealed (for 300 s at 953 K and 1093 K) states.

though no hard magnetic characteristics are obtained for the melt-spun amorphous phase. The I_r, $_iH_c$ and $(BH)_{max}$ show maximum values in the T_a range above 1070 K corresponding to the temperature range above the fourth exothermic peak at the DSC curves. The I_s, I_r, $_iH_c$ and $(BH)_{max}$ values at the annealing condition where the maximum $(BH)_{max}$ is obtained are 1.18 T, 0.75 T, 58 kA/m and 13 kJ/m^3, respectively, for the 4%Zr alloy and 1.15 T, 0.76 T, 30 kA/m and 7.8 kJ/m^3, respectively, for the 6%Zr alloy. As an example, the hysteresis I-H loops of the as-quenched and annealed $Fe_{63}Co_7Nd_6Zr_4B_{20}$ alloy are shown in Fig. 7. The annealing changes the magnetic properties from soft to hard type, and the hysteresis I-H loop has a very smooth shape without any appreciable step. Besides, we confirmed the reversible phenomenon of the demagnetization curve in reverse magnetic fields. The features of the hysteresis I-H loop agree with those for B-rich Fe–Nd–B alloys consisting mainly of Fe_3B and $Nd_2Fe_{14}B$ phases[32]. The agreement suggests that the hard magnetic properties are due to the exchange magnetic coupling interaction[33] between α-Fe and $Nd_2Fe_{14}B$ phases even in the coexistent state with Fe_2Zr, Fe_3Zr, Fe_2B and ZrB_2 phases.

The microstructure and alloy component of the constituent phases were examined for the Fe–Co–Nd–Zr–B alloys by high-resolution TEM, nanobeam electron diffraction and nanobeam EDX analyses. Figure 8 shows the high-resolution TEM image and nanobeam electron diffraction patterns of regions A, B, C and D for the $Fe_{63}Co_7Nd_6Zr_4B_{20}$ alloy annealed for 300 s at 1093 K. The electron diffraction patterns were identified to be of α-Fe for the region A, of $Nd_2Fe_{14}B$ for region B, of Fe_3Zr for the region C and of Fe_2Zr for the region D. The

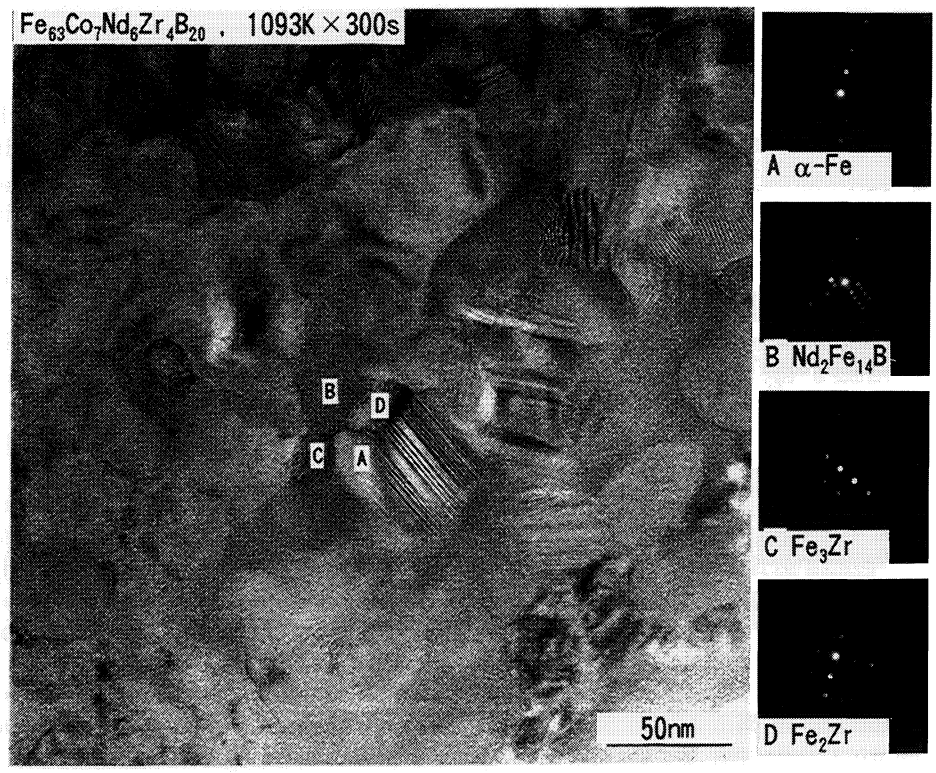

Fig. 8 High resolution TEM image and nanobeam electron diffraction patterns taken from the small areas with a diameter of 3 nm in the grains A, B, C and D for an amorphous $Fe_{63}Co_7Nd_6Zr_4B_{20}$ alloy annealed for 300 s at 1093 K.

average grain size is about 40 nm for α-Fe and about 25 nm for the other three phases, indicating that the coexistence of the Fe_3Zr and Fe_2Zr phases maintains the nanoscale structure. The analytical compositions of the metallic components without boron obtained from the EDX profiles are also summarized in Table 1. Their analytical compositions correspond roughly to the stoichiometric compositions of the four phases. The present TEM result is consistent with that obtained by X-ray diffractometry. The crystallites are composed of multiple phases and the structure is too complex for determining the interparticle spacings among the constituent phases. It is expected that the small grain sizes of the constituent phases can lead to an appropriate structure in which the interparticle spacings are small enough to cause the hard magnetic properties through the exchange magnetic coupling interaction.

Table 1 Analytical alloy compositions of the grains A, B, C and D in an amorphous $Fe_{63}Co_7Nd_6Zr_4B_{20}$ alloy annealed for 300 s at 1093 K. The analysis was made by nanobeam EDX spectroscopy and assumed to be 100% for the mixture of Fe, Co, Nd and Zr elements.

Metallic component		Fe	Co	Nd	Zr
Region	Phase	at%			
A	α-Fe	92.85	6.65	0.33	0.26
B	$Nd_2Fe_{14}B$	70.71	14.87	14.04	0.38
C	Fe_3Zr	63.96	10.63	1.10	24.31
D	Fe_2Zr	54.80	10.66	2.31	32.23

IV. Discussion

1. Formation of the new crystalline phases

It was shown that the fully crystalline structure consisted mainly of α-Fe, Fe_2Zr, $Nd_2Fe_{14}B$ and ZrB_2 for the $Fe_{63}Co_7Nd_6Zr_4B_{20}$ and $Fe_{63}Co_7Nd_4Zr_6B_{20}$ alloys, which are significantly different from Fe_3B, $Nd_2Fe_{14}B$ and α-Fe for $Fe_{75}Nd_5B_{20}$. The addition of Zr causes the precipitation of additional Fe_2Zr and ZrB_2 phases. The Fe_3B phase appears as an intermediate metastable phase. It has been reported[34] that the predicted negative heat of mixing is 23 kJ/mol for Fe_3B, 34 kJ/mol for Fe_2Zr and 98 kJ/mol for ZrB_2, and the melting temperature and/or decomposition temperature is 1525 K for Fe_3B, 1946 K for Fe_2Zr and 3313 K for ZrB_2[35]. The bonding nature increases in the order of $ZrB_2 > Fe_2Zr > Fe_3B$. The generation of the Zr–B and Fe–Zr stronger bonding pairs by the addition of Zr leads to the precipitation of Fe_2Zr and ZrB_2 phases. The change in the crystallization behavior also implies that the generation of the strongly bonding Fe–Zr and Zr–B pairs plays an important role in the appearance of the glass transition and supercooled liquid region before crystallization. That is, the generation of the strongly bonding Zr–B and Fe–Zr pairs increases the viscosity and the difficulty of crystallization by hindering the atomic rearrangement. The high precipitation tendency of Fe_3B as a primary phase is presumably due to the higher atomic diffusivity of Fe and B atoms as compared with Zr. The increase in the atomic diffusivity of

Zr at the higher temperature above 1070 K enables the formation of Zr_2B and Fe_2Zr phases, accompanying the decomposition of Fe_3B.

2. The glass transition and the supercooled liquid region

The supercooled liquid of the $Fe_{63}Co_7Nd_{10-x}Zr_xB_{20}$ (x=4 and 6 at%) alloys has a high resistance against crystallization which induces the appearance of the glass transition. It is therefore important to investigate the reason why this supercooled liquid has high resistance against crystallization. According to the three empirical rules for the achievement of high glass-forming ability, we investigate the atomic sizes and the heats of mixing among the constituent elements. The atomic size changes in the order of Nd≫Zr≫Co>Fe≫B[36]. The predicted heat of mixing is 34 kJ/mol for equiatomic Fe–Zr pair, 38 kJ/mol for Fe–B pair, 60 kJ/mol for Co–Zr pair and 34 kJ/mol for Co–B pair[34], respectively. The three empirical rules for the achievement of high glass-forming ability are well satisfied for the $Fe_{63}Co_7Zr_{10}B_{20}$ alloy, which seems to be the reason for the appearance of the wide supercooled liquid region with ΔT_x of 58 K. It has previously been reported[37]-[39] that the satisfaction of the three empirical rules causes the formation of a higher degree of dense random packed amorphous structure and a new local atomic configuration which is different from those for the corresponding equilibrium compounds. This type of amorphous structure has a lower atomic diffusivity, a higher viscosity and a smaller specific volume. Furthermore, it is well known[17]-[19] that this multicomponent amorphous alloys crystallize through a single exothermic peak due to the simultaneous precipitation of more than three crystalline phases, Fe_3B, α-Fe and Fe_2Zr. This crystallization mode indicates the necessity of the long-range atomic rearrangements which are difficult for the unique amorphous structure of the multicomponent alloys. The unique amorphous structure and the single-stage crystallization mode induce high resistance of the supercooled liquid against crystallization, leading to the appearance of the wide supercooled liquid region. The additional Nd element has the similar negative heats of mixing with Fe, Co and B because of the existence of various intermetallic compounds at an equilibrium state[35]. However, the values of Nd–M (M=Fe, Co or B) pairs are much smaller than those for the Zr–M pairs. The much weaker bonding nature seems to decrease the resistance of supercooled liquid against crystallization, leading to the disappearance of the glass transition and supercooled liquid region. Besides, it is presumed that the attractive bonding state leading to the wide supercooled liquid region is retained in the concentration range below 6 at%Nd. The generation of the weak bonding pairs by the addition of Nd also may be the reason for the change in the crystallization mode from the single stage for the Fe–Co–Zr–B alloy to the three stages for the Fe–Co–Zr–Nd–B alloy.

V. Summary

With the aim of synthesizing a bulk hard magnetic alloy by annealing cast bulk amorphous alloys, a new amorphous alloy in the $Fe_{63}Co_7Nd_{10-x}M_xB_{20}$ (M=Zr or Nb, x=0 to 6) system was found of which the glass transition, supercooled liquid region and the hard magnetic crystallized structure are observed. The results obtained are summarized as follows.

(1) The 4%Zr- and 6%Zr-containing alloys exhibit the glass transition, followed by a supercooled liquid region before crystallization. The T_g and T_x are 844 and 877 K respectively for the 4%Zr alloy, and 839 and 880 K for the 6%Zr alloy.

(2) The crystallization from the supercooled liquid for the 4% alloy takes place through three stages of Am $\rightarrow$Am′ + Fe_3B $\rightarrow$Am″ + Fe_3B + γ-Fe + $Nd_2Fe_{23}B_3$ + Fe_2Zr + Fe_3Zr $\rightarrow$$\alpha$-Fe + Fe_2Zr + Fe_3Zr + $Nd_2Fe_{14}B$ + Fe_2B + Zr_2B. The average grain size is about 40 nm for α-Fe and about 25 nm for $Nd_2Fe_{14}B$, Fe_2Zr and Fe_3Zr.

(3) The hard magnetic properties are obtained at the fully crystallized state for the 4% and 6%Zr alloys. The maximum hard magnetic characteristics are 1.18 T for I_s, 0.75 T for I_r, 58 kA/m for ${}_iH_c$ and 13 kJ/m^3 for $(BH)_{max}$ for the 4%Zr alloy annealed for 300 s at 1093 K.

(4) The hard magnetic properties are presumably due to the exchange magnetic coupling interaction between α-Fe and $Nd_2Fe_{14}B$ phases in the nanoscale mixed structure. The finding of the alloys exhibiting simultaneously the glass transition and supercooled liquid region at the amorphous state and hard magnetic properties at the crystallized state is important for the future development of a bulk hard magnetic alloy which is synthesized by casting and subsequent annealing.

Acknowledgment

One of the authors (A. Inoue) is grateful to the Grant-in-Aid for Specially Promoted Research of the Ministry of Education, Science, Sports and Culture of Japan for support of this research.

REFERENCES

(1) R. C. Crewdson: Calif. Tech. Rep., **CALT-221-20** (1966), 21.
(2) P.L. Maitrepierre: J. App. Phys., **40** (1969), 4826.
(3) H. S. Chen: Rep. Prog. Phys., **43** (1980), 353.
(4) A. Inoue, T. Zhang and T. Masumoto: Mater. Trans., JIM, **30** (1989), 965.
(5) A. Inoue, H. Yamaguchi, T. Zhang and T. Masumoto: Mater. Trans., JIM, **31** (1990), 104.
(6) A. Inoue, K. Ohtera, K. Kita and T. Masumoto: Jpn. J. Appl. Phys., **27** (1988), L2248.
(7) A. Inoue, M. Kohinata, A.P. Tsai and T. Masumoto: Mater. Trans., JIM, **30** (1989), 378.
(8) A. Inoue, T. Zhang and T. Masumoto: Mater. Trans., JIM, **31** (1990), 177.
(9) T. Zhang, A. Inoue and T. Masumoto: Mater. Trans., JIM, **32** (1991), 1005.
(10) A. Inoue, T. Shibata and T. Zhang: Mater. Trans., JIM, **36** (1995), 1420.
(11) A. Peker and W.L. Johnson: Appl. Phys. Lett., **63** (1993), 2342.
(12) A. Inoue, N. Nishiyama and T. Matsuda: Mater. Trans., JIM, **37**

(1996), 181.
(13) A. Inoue, T. Nakamura, T. Sugita, T. Zhang and T. Masumoto: Mater. Trans., JIM, **34** (1993), 351.
(14) S. G. Kim, A. Inoue and T. Masumoto: Mater. Trans., JIM, **31** (1990), 929.
(15) A. Inoue, T. Nakamura, N. Nishiyama and T. Masumoto: Mater. Trans., JIM, **33** (1992), 937.
(16) A. Inoue and T. Zhang: Mater. Trans., JIM, **37** (1996), 185.
(17) A. Inoue and N. Nishiyama: Mater. Trans., JIM, **38** (1997), 179.
(18) A. Inoue: Mater. Trans., JIM, **36** (1995), 866.
(19) A. Inoue: Sci. Rep. Res. Inst. Tohoku Univ., **A42** (1996), 1.
(20) A. Inoue: Mater. Sci. Eng., **A226-228** (1997), 357.
(21) A. Inoue: Mater. Sci. Forum, **179-181** (1995), 691.
(22) A. Inoue: Nanostructured and Non-Crystalline Materials, ed. by M. Vazquez and A. Hernanodo, World Scientific, Singapore, (1994), p. 15.
(23) A. Inoue: *Advanced Materials and Processing*, ed. by K. S. Shin, J. K. Yoon and S. J. Kim, The Korean Inst. Metals and Materials, Seoul, (1995), p. 1849.
(24) A. Inoue and J.S. Gook: Mater. Trans., JIM, **36** (1995), 1180.
(25) A. Inoue, A. Takeuchi, T. Zhang, A. Murakami and A. Makino: IEEE Trans. Mag., **32** (1996), 4866.
(26) A. Inoue, T. Zhang, T. Itoi and A. Takeuchi: Mater. Trans., JIM, **38** (1997), 358.
(27) A. Inoue, H. Koshiba, T. Zhang and A. Makino: Mater. Trans., JIM, **38** (1997), 577.
(28) A. Inoue, T. Zhang and A. Takeuchi: Appl. Phys. Lett., **71** (1997), 464.
(29) H.S. Chen: Rep. Prog. Phys., **43** (1980), 353.
(30) K. Nagayama, H. Ino and T. Umeda: J. Japan Inst. Metals, **54** (1990), 720.
(31) S. Hirosawa, H. Kanekiyo and M. Uehara: J. Appl. Phys., **73** (1993), 6488.
(32) E. F. Kneller and R. Hawig: IEEE Trans. Magn., **27** (1991), 3588.
(33) K. H. J. Buschow, D. B. de Mooij and H. M. van Noort: J. Less-Common Metals, **125** (1986), 135.
(34) F. R. de Boer, R. Boom, W. C. M. Mattens, A. R. Miedema and A. K. Niessen: *Cohesion in Metals*, Elsevier Science Publishers, North-Holland, (1988), p. 227.
(35) *Binary Alloy Phase Diagrams*, ed. by T. B. Massalski, ASM International, Materials Park, Ohio, (1990), p. 480.
(36) *Metals Databook*, ed. by Japan Inst. Metals, Maruzen, Tokyo, (1983), p. 8.
(37) E. Matsubara, T. Tamura, Y. Waseda, A. Inoue, M. Kohinata and T. Masumoto: Mater. Trans., JIM, **31** (1990), 228.
(38) E. Matsubara, T. Tamura, Y. Waseda, A. Inoue, T. Zhang and T. Masumoto: Mater. Trans., JIM, **33** (1992), 873.
(39) E. Matsubara, T. Tamura, Y. Waseda, T. Zhang, A. Inoue and T. Masumoto: J. Non-Cryst. Solids, **150** (1992), 380.